

Armstrong liquid bridge: Formation, evolution and breakupXueqin Pan, Man Hu, Bingrui Xu, Feng Wang, Peng Huo, Fangqi Chen,
Zhibo Gu, and Daosheng Deng^{✉*}*Department of Aeronautics and Astronautics, Fudan University, Shanghai 200433, China*

(Received 16 December 2020; accepted 18 August 2021; published 2 September 2021)

In this paper, we experimentally explore the formation, evolution, and breakup of the Armstrong liquid bridge. The extremely complicated evolution stage is revealed, which involves many coupled processes including the morphology change, current variation, heat transfer, and water evaporation. By focusing on the final fate of this liquid bridge, we observe that the breakup occurs once an effective length (\bar{L}) is reached. This effective length increases linearly with the applied voltage, implying a threshold electric field to sustain the liquid bridge. Moreover, by an introduced external flow, the lifetime of the liquid bridge can be controlled, while the effective length associated with the breakup is independent of the external flow rate. Hence, these findings remarkably demonstrate that the breakup of the liquid bridge is directly correlated with the effective length. In order to understand this correlation, a simplified model of an electrified jet is employed to take the electric field into account. By the linear stability analysis, the attained phase diagram agrees with the experiments well. Although a more comprehensive theory is required to consider other factors such as the surface charges, these results might provide a fresh perspective on the “century-old” Armstrong liquid bridge to further elucidate its underlying physical mechanism.

DOI: [10.1103/PhysRevFluids.6.093901](https://doi.org/10.1103/PhysRevFluids.6.093901)**I. INTRODUCTION**

In 1893, W. G. Armstrong discovered a fascinating observation of “a rope of water suspended between the lips of the two glasses” under an applied voltage [1]. Recently, this Armstrong liquid bridge (ALB) has been revisited with advanced experimental tools, such as the high-speed camera to reveal its rapid formation dynamics [2–4]. This system is extremely complicated, involving the coupled physical processes (EHD, heat transfer, and mass transport [5]) and the undesirable chemical reactions (water splitting at the electrodes and the production of protons [6,7], and the change of pH [8,9]).

One of the distinctive features is that the Armstrong liquid bridge floats horizontally or hangs stably between the two beakers without much deflection vertically in a gravity-defying fashion. This feature has been extensively studied using a simple classical electro-hydrodynamics (EHD) theory [10,11]. Both the surface tension and Maxwell stress can provide the upward forces to counteract the downward gravitational force, in order to hold the ALB [12–14].

Another intriguing feature is that the Armstrong liquid bridge can persist or be stable for a while up to tens of minutes [4]. However, the final fate of the Armstrong liquid bridge (the breakup and the associated lifetime), which is essential to elucidate the underlying physical mechanism for its stability or persistence, has not been thoroughly investigated at a quantitative level in the literature, to the best of our knowledge.

*dsdeng@fudan.edu.cn

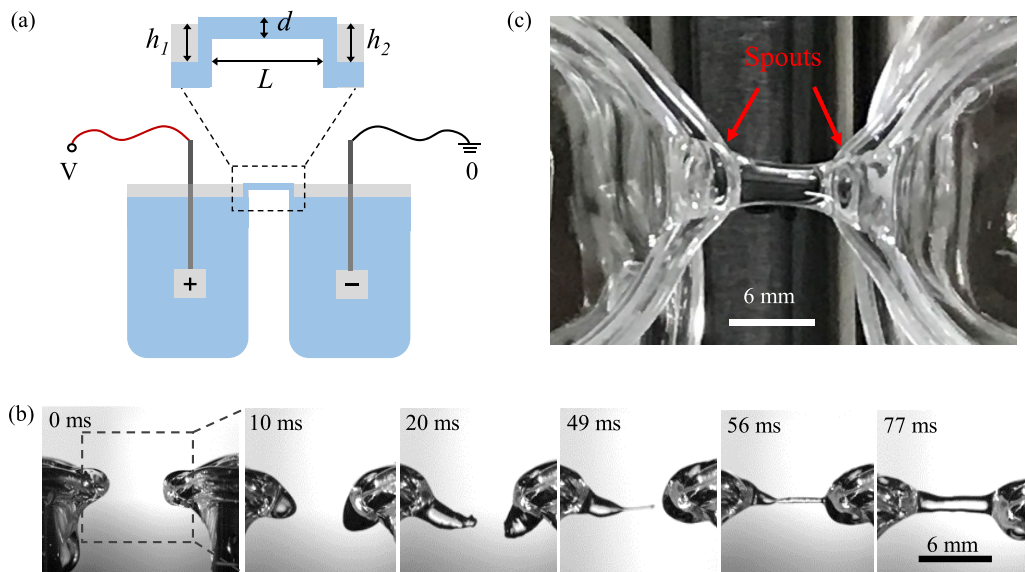


FIG. 1. Formation of the ALB. (a) The sketch of the experimental setup and a magnified view of the ALB suspended between beakers with their small spouts facing closely (V for the applied voltage, L for the distance between the two spouts, $d = 2r_0$ for the diameter, h_1 and h_2 for the climbing height, and the cylindrical beakers with 3.2 cm diameter and 5 cm height). (b) High-speed images for the initial formation of the ALB from a side view ($L = 6$ mm, $V = 13$ kV). (c) A top view of the liquid bridge.

In this work, we focus on the stability of the floating bridge from the perspective of its final fate in terms of its lifetime once the breakup appears, and highlight three main findings. First, the breakup occurs once an effective length (\tilde{L}) is reached under a given voltage. Remarkably, this effective length has a simple linear relationship with the applied voltage. Second, by introducing an external flow, the lifetime of the liquid bridge can be controlled, while the effective length associated with the breakup is independent of the flow rate. Third, in order to understand the observed correlation between an effective length and breakup, a theoretical model is employed and the linear stability analysis agrees with experiments well.

The paper is organized as follows. In Sec. II, the initial formation of ALB arises from the emission and connection of Taylor-cone jets. In Sec. III, the extremely complicated evolution stage is revealed, which involves many coupled processes, such as the morphology change, current variation, heat transfer, and water evaporation. Then in Sec. IV, the occurrence of the breakup is found to be correlated with an effective length (\tilde{L}). In Sec. V, an external flow is introduced to manipulate the liquid bridge and its lifetime (τ_{lifetime}), but the effective length associated with the breakup is unaffected by the external flow. In Sec. VI, a model of an electrified jet is proposed by taking the electric field into account, and a phase diagram is obtained to compare with the experiments. Lastly, the discussion and outlook for the ALB are provided in Sec. VII.

II. FORMATION OF THE ALB: EMISSION AND CONNECTION OF TAYLOR-CONE JETS

As shown in the sketch of Fig. 1(a), two cylindrical beakers (with the diameter and height about 3.2 cm and 5 cm, respectively) are filled with the deionized water (Shanghai Dienna Biotechnology Co., Ltd.), and separated with a distance L about millimeters with their small spouts facing each other closely in the opposite direction. An external voltage (V) through a high-voltage power supplier (DW-P303-5ACF 1) is applied between the beakers through platinum electrodes immersed

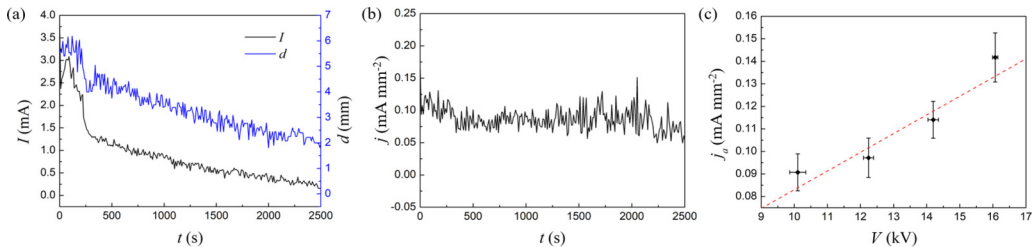


FIG. 2. Current density. (a) The simultaneous measurement of current and diameter ($V = 12$ kV, $L = 6$ mm). (b) Current density j fluctuating over the time. (c) The measurement of j_a (the black dots) agreeing with the calculation from the Ohm's law (the red dashed line). Error bars from four measurements.

into water. More details of the experimental setup, procedures, and operation safety have been described as well [15].

As the voltage is gradually increased to a critical voltage (V_c) on the order of kV, the initial formation of the ALB is revealed by the high-speed images (Phantom V611) (Fig. 1(b) for a side view, and see Supplemental Material [16] for Video 1). Because of the gradual charge accumulation in water near the spouts under the applied voltage, water climbs or creeps to the spouts of the beakers, generating the inception of Taylor cones ($t = 10$ ms) [17]. Then around 20 ms, the Taylor cones are subjected to the strong electric field, resulting in their deformation or extension. Around 49 ms, a fine jet is emitted horizontally away from one of the Taylor cones, leading to a cone-jet structure [18]. Once the jet from the left beaker connects to the right beaker around 56 ms, a liquid bridge floats between the two beakers, while its diameter ($d = 2r_0$ measured at the center of the liquid bridge) increases shortly. Eventually around 77 ms, the liquid bridge has been fully developed and reaches a stable state with the diameter around millimeters, as shown in Fig. 1(c) (a top-down view from a digital camera, Nikon D7200 with the lens of AF-S DX NIKKOR 16–85 mm). The linear increase of V_c with L indicates that a critical electric field is required to initiate the formation of the ALB ($E_{\text{formation}} \approx 1$ kV mm⁻¹) (Appendix A).

III. EVOLUTION OF THE ALB

In contrast to the extremely fast process within tens of milliseconds during the initial formation [2,4,19], the ALB can persist or be sustained for a much longer period, up to tens of minutes. This evolution process is extremely complicated and systematically investigated here, including the current, heat transfer, mass transfer, mass loss, and climbing heights.

A. Current and diameter

Once the liquid bridge is initiated, the water in the two beakers is connected by the liquid bridge to form an electric circuit under the applied voltage, generating the electric current. Current (I) changes with time, while the morphology and the associated diameter of the liquid bridge evolves with time as well [Fig. 2(a) for $V = 12$ kV]. The current and diameter have a certain correlation: The smaller (larger) diameter has the higher (lower) resistance of the liquid bridge and the smaller (larger) current. Indeed, in the experiments, the current density ($j = I/A$) fluctuates over the time around the time-averaged current density ($j_a \approx 0.1$ mA mm⁻²), as shown in Fig. 2(b).

Additionally, j_a has a tendency to increase with the applied voltage [Fig. 2(c)]. From the Ohm's law,

$$j_a = \sigma E \propto V, \quad (1)$$

where $\sigma = 0.5$ $\mu\text{S cm}^{-1}$ is the conductivity of deionized water. Then the calculated j_a (the red dashed line) fits well with experimental data [Fig. 2(c)], indicating that the voltage is mainly dropped

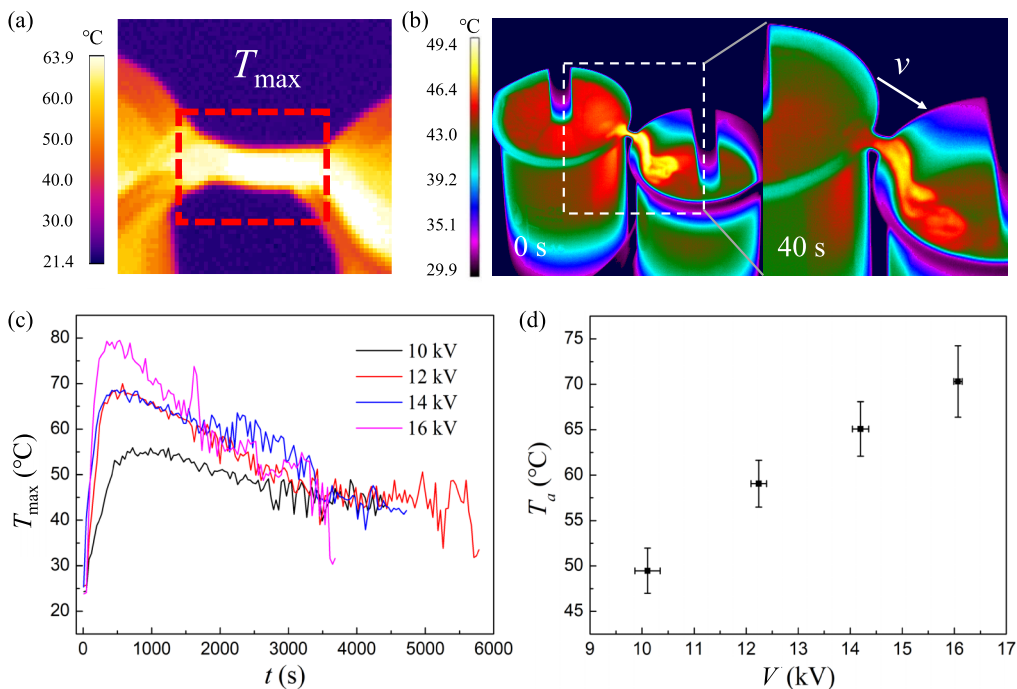


FIG. 3. Temperature evolution. (a) Thermal image of the ALB ($V = 12$ kV, $L = 6$ mm). (b) Thermal images revealing a waterfall falling from the liquid bridge to one of the beakers and the corresponding temperature distribution. (c) T_{\max} changing over time under different voltages. (d) T_a increasing with the applied voltages (error bars for four measurements).

in the liquid bridge. Since the resistance (proportional to the ratio between the length of the liquid bridge and the area of its cross section) of the liquid bridge is nearly 3 orders of magnitude higher than that of water in the beakers by estimating the geometric length scale, the voltage is reasonably expected to be dropped along the liquid bridge.

B. Heat transfer and temperature evolution

Since the two beakers are connected by the ALB, the water temperature [Figs. 3(a) and 3(b)] is elevated due to the Joule heating, and is revealed by thermal images from the thermal camera (FLIR A6752sc). The temperature of the liquid bridge is characterized by its maximum value along the liquid bridge (T_{\max}), as indicated by Fig. 3(a). The evolution of T_{\max} and its dependence on V are shown in Fig. 3(c). T_{\max} reaches its peak within ten minutes after connection and then begins to decrease gradually due to the effect of evaporation and heat dissipation. The time-averaged temperature (T_a) increases with the applied voltage [Fig. 3(d)]. Although a part of the infrared emission of the liquid bridge might come from the proton conduction [20], the infrared emission in the thermal images is mainly attributed to the Joule heating.

C. The reduction of water level and the increase of the climbing height

During the evolution stage, the surface level of water (red lines) in the beakers is gradually diminished about several millimeters (Fig. 4(a) and see Supplemental Material [16] for Video 2). Figure 4(b) presents the change of the climbing height (the distance between the rim or the upper edge of the beaker and the water level, referring to the creeping height in [5]) at the anode (h_1) and cathode side (h_2) [as shown in Fig. 1(a) and Fig. 4(a)]. The variations of h_1 and h_2 [in Fig. 1(a)]

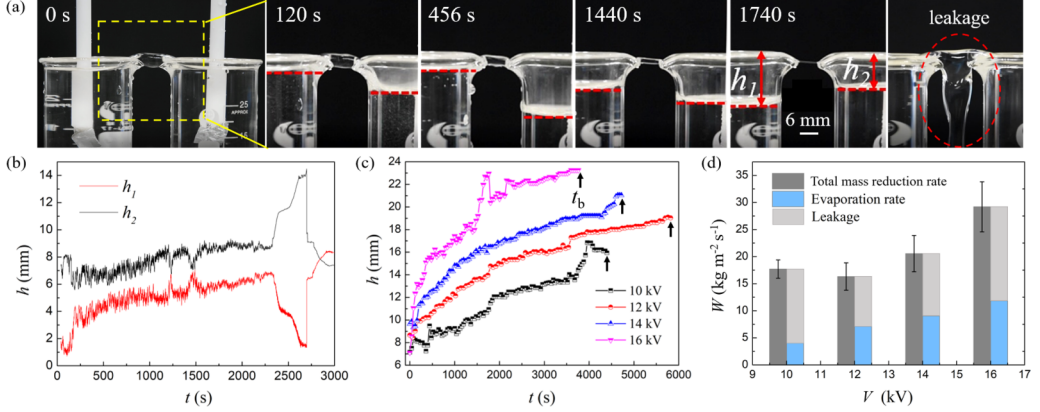


FIG. 4. Mass loss characterized by the reduced water level or the increased climbing height. (a) Photographs showing the change of water level (red dashed lines) inside the beakers with time, and the inadvertent leakage ($L = 6$ mm, $V = 16$ kV). (b) The climbing height of water level in two beakers at the anode side (h_1) and the cathode side (h_2) changing with time. (c) The total climbing height ($h = h_1 + h_2$) increasing with time for various voltages. (d) The mass reduction of water due to the evaporation and the leakage (error bars for four measurements).

is caused by an axial flow of the liquid bridge between the two beakers, forming a waterfall [see Supplemental Material [16] for Video 3 and Fig. 3(b)]. This axial flow can be bidirectional, flowing from the anode (cathode) side to the cathode (anode) side between the beakers during the evolution [9,21]. The velocity of this axial flow is on the order of tens of millimeters per second (more details in Appendix B).

Then the reduction of the water level is characterized by the total climbing height ($h = h_1 + h_2$). As presented in Fig. 4(c), h gradually increases with time for various applied voltages until the final breakup time (t_b). This reduction of water level corresponds to the total mass loss of water in the beakers.

D. Mass loss: Evaporation and leakage

As shown in Fig. 4(d), this average reduction rate of total mass (W , the dark shadow) is attributed to the evaporation (the blue shadow) and leakage (the light shadow). The evaporation of water inside the beakers increases with the applied voltage due to Joule heating. Based on the measured temperature, the evaporation rate [Fig. 4(d)] is theoretically estimated from Dalton's evaporation law [22],

$$E = A \left[\frac{P(T_w)}{T_w} - \frac{HP(T_0)}{T_0} \right], \quad (2)$$

where E is the evaporation rate, T_w is the temperature of the water surface, T_0 is the temperature of the air atmosphere, $P(T)$ is the vapor pressure at temperature T , and H is the relative humidity in the air. A is a constant dependent on the air velocity and temperature in experiments (0.3 m s^{-1} and 22°C). Here the time-averaged temperature (T_a) in Fig. 3(d) is approximately used as T_w . The calculated evaporation rate under the applied voltage is about 1/3 of the averaged rate of the total mass change [Fig. 4(d)].

The leakage of water takes place inadvertently during the evolution of the liquid bridge, as shown by the right snapshot in Fig. 4(a) and Video 2 of the Supplemental Material [16]. Once water falls from the beakers or the liquid bridge down to the ground due to the gravity, the total mass of water (in the breakers and within the liquid bridge) is reduced accordingly, resulting in the change of the

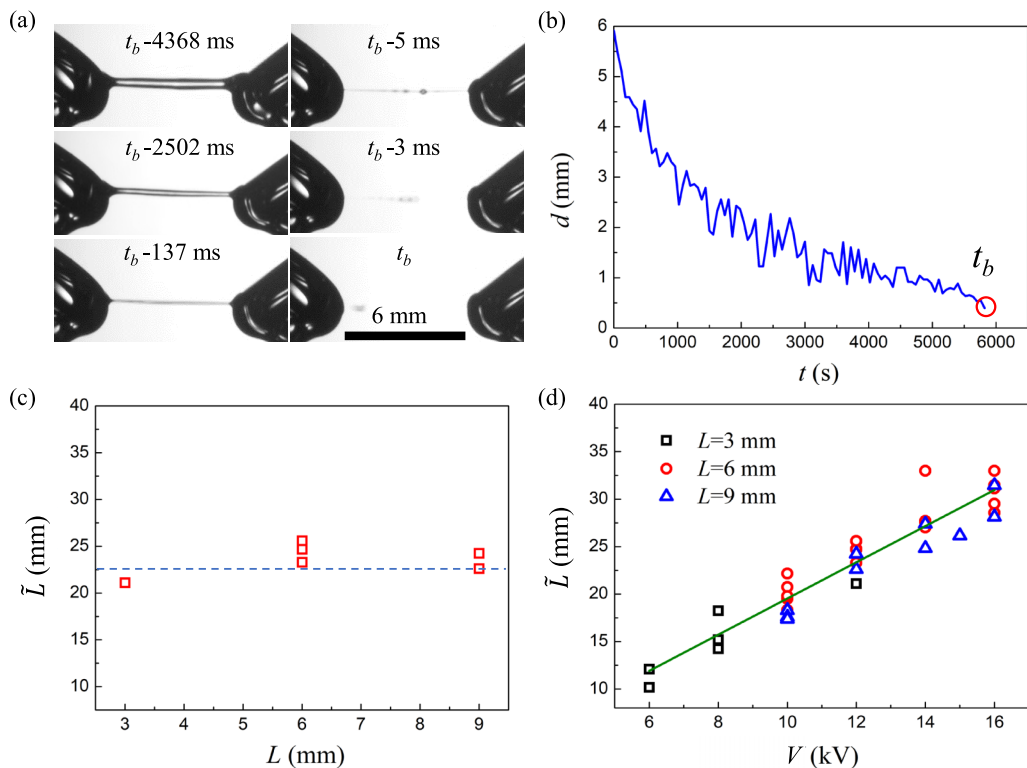


FIG. 5. Breakup of the ALB. (a) High-speed images of the typical breakup ($L = 6$ mm, $V = 12$ kV). (b) Diameter of bridge gradually decreasing until the final breakup. (c) At the breakup time (t_b), $\tilde{L} = h(t_b) + L$ almost a constant for various L ($V = 12$ kV). (d) Experimentally \tilde{L} increasing linearly with V for various L , and its slope indicating a constant electric field $E_{\text{breakup}} = 0.52$ kV mm $^{-1}$ associated with the breakup.

total climbing height. The leakage of water during the complicated evolution process of the ALB takes place inadvertently or accidentally, and it is difficult to be predicted theoretically or described accurately due to its uncertain occurrence. Based on the assumption that the mass loss is due to the evaporation and leakage, the average leakage rate is obtained by subtracting the evaporation rate from the average rate of mass reduction. As shown in Fig. 4(d), the average rate of the leakage is about 2/3 of the averaged rate of the total mass reduction.

IV. BREAKUP OF THE ALB

Therefore, the gradual loss of water manifestly causes the continuous increase of h , and eventually results in the final fate of the breakup (Figs. 5(a) and 5(b), and see Supplemental Material [16] for Video 4).

A. Breakup dynamics

As captured by the high-speed images [Fig. 5(a)], the continuous liquid bridge within the last several seconds is rapidly thinned to an extremely tiny filament to be more susceptible to the instability, eventually breaking up into a series of tiny droplets within the last five milliseconds.

During the whole course of the ALB, the diameter of the liquid bridge is decreased from six millimeters at the initial stage down to hundreds of micrometers approaching the breakup [Fig. 5(b)], as limited by the resolution of the high-speed camera experimentally. Although the radius near the

spouts of the beakers at the initial stage depends on the electric field [5,14], this time-dependent diameter of the ALB requires future investigation.

B. An effective length (\tilde{L})

For a given voltage ($V = 12$ kV), by carrying out a series of experiments, we find at breakup time t_b that the total climbing height $h(t_b)$ decreases with L . Then an effective length is simply defined as follows,

$$\tilde{L} = h(t_b) + L. \quad (3)$$

As shown in Fig. 5(c), this effective length (\tilde{L}) is nearly a constant or independent of the distance between beakers, L . In other words, at a shorter L , the breakup occurs at a larger $h(t_b)$, while at a longer L , the breakup occurs for a smaller $h(t_b)$. This reproductivity of the effective length is striking in the final fate of liquid bridge, considering such complicated evolution processes and uncertain factors such as the leakage.

Moreover, we perform a series of experiments to investigate both L and V together, and identify $h(t_b)$ at the final breakup time. Noticeably, all the data of the effective length [$\tilde{L} = h(t_b) + L$] and V [Fig. 5(d)] linearly collapse into a master line. Considering the complicated system of the liquid bridge under a high voltage (involving the heat transfer, flow, evaporation, the occasional leakage, and the chemical reactions), this correlation between an effective length and the voltage at the final fate of Armstrong liquid bridge is remarkable.

V. MANIPULATION OF THE ALB VIA AN EXTERNAL FLOW

In order to further validate the crucial role of the effective length at the final fate of the ALB, an external flow is introduced to manipulate the change of water level and the associated lifetime.

A. \tilde{L} independent of the flow rate

Water is extracted out of the beakers through syringe pumps (Ristron RSP04-BD) [Fig. 6(a)]. Each syringe (5 ml in volume) is pushed or pulled automatically at a given flow rate. One end of PTFE soft pipes is connected to the syringe, while the other end is immersed into water in beakers. In this way, the water can be extracted out of or injected into the beakers under various flow rates during the ALB experiments.

For a given voltage ($V = 14$ kV), the time-dependent $h + L$ under different rates of extraction flow is presented in Fig. 6(b), and again the value of $h + L$ at the final breakup time $\tilde{L} = h(t_b) + L$ is nearly a constant [Fig. 6(c)].

B. Reduced τ_{lifetime} via flow extraction

The extraction flow correspondingly causes the increased $h + L$, resulting in the decreased τ_{lifetime} [Fig. 6(d)]. Actually, this effect of external flow rate on τ_{lifetime} can be estimated from the reduction of the mass by considering the evaporation rate (C_e), the flow rate of extraction (f), and the leakage mass (ΔC). For the case without the flow extraction, $\Delta m = \Delta C + C_e \tau_0$, where Δm is the total mass reduction of water during the whole experiment, C_e is the evaporation rate, and τ_0 is the lifetime without extraction. Then for the case with the flow extraction, $\Delta m = \Delta C + C_e \tau + f \tau$, where f is the extraction rate, and τ is the associated lifetime.

Despite the different extraction rates, when the beaker distance L and the applied voltage V are fixed, the total height or mass change is nearly a constant once the breakup occurs. Thus the total mass reduction Δm is supposed to be the same in both cases. Under an assumption of a constant leakage ΔC , the relation between τ and f is obtained as follows,

$$\tau_{\text{lifetime}} = C_e \tau_0 / (C_e + f). \quad (4)$$

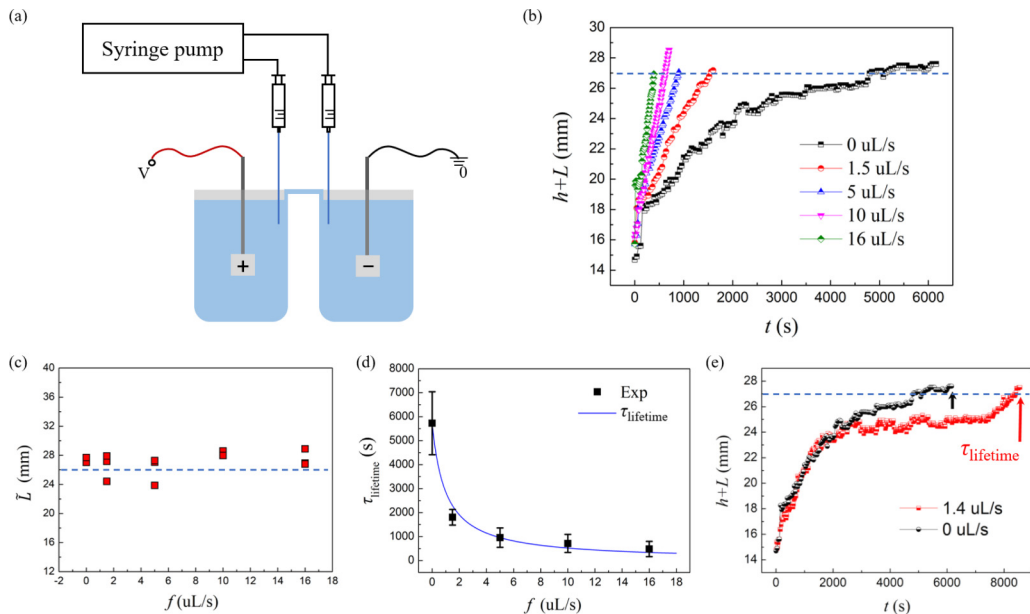


FIG. 6. Control of the ALB by an external flow. (a) The sketch of manipulating liquid bridge by an external flow through a syringe pump. (b) The evolution of $h + L$ with time under various flow rates. (c) The similar $\tilde{L} = h(t_b) + L$ upon breakup, nearly independent on the flow rate. (d) The reduction of τ_{lifetime} by the flow extraction, the experimental data (black squares, error bars for three measurements) fitted well by τ_{lifetime} : Eq. (4) (the blue line). (e) The extension of τ_{lifetime} over two hours by flow injection ($V = 14 \text{ kV}$, $L = 6 \text{ mm}$).

The above equation states that the lifetime τ is related with an evaporation rate C_e and the applied extraction rate f . Indeed, the experimental data can be fitted well with Eq. (4) [the blue line in Fig. 6(d)].

C. Extended τ_{lifetime} via flow injection

Conversely, by supplying water into beakers through injection to balance the water loss due to evaporation or leakage, the level of water surface is slowly changed, consequently taking a longer time to reach \tilde{L} or extending the lifetime of liquid bridge. Figure 6(e) shows the evolution of $h + L$ without an external flow and with an injection flow rate at $1.4 \mu\text{L s}^{-1}$. At the beginning from 0 to 2000 seconds, the injection has less effect on the climbing height. Between 2000 s and 7000 s, $h + L$ increases slowly due to the injection of water. However, after 7000 seconds as the water in the syringe is used up, $h + L$ starts to increase fast due to the evaporation and leakage. Clearly, τ_{lifetime} has been extended longer than 2 hours with an injection rate. For both cases, breakup occurs when \tilde{L} reaches around 27 mm.

VI. A THEORETICAL MODEL

The final fate of the Armstrong liquid bridge has been experimentally characterized by the effective length, \tilde{L} , which is independent of the beaker distance [Fig. 5(c)] and the external flow rate f [Fig. 6(c)]. Remarkably, \tilde{L} linearly increases with the voltage V [Fig. 5(d)], and its slope implies an electric field $E_{\text{breakup}} \approx 0.52 \text{ kV mm}^{-1}$, below which the liquid bridge will experience the instability and be subjected to the breakup. In other words, a sufficiently strong electric field might be necessary, if not sufficient, to maintain the liquid bridge or sustain its stability.

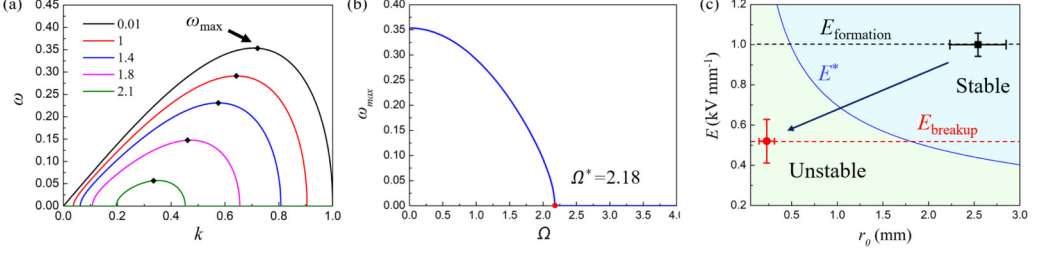


FIG. 7. Linear stability analysis. (a) The dispersion relationship or the growth rate ω dependent on the wavelength k under different dimensionless electrical field Ω . $\Omega = 0.01, 1, 1.4, 1.8, 2.1$ from the outer line to the inner line, and ω_{\max} for the maximum of ω . (b) The dispersion relationship ($\omega_{\max} - \Omega$) showing a critical value of the dimensionless electric field ($\Omega^* = 2.18$). (c) The calculated phase diagram ($E - r_0$) consistent with the experimental observation. The dark square for the initial formation, while the red circle for the final breakup (error bars from experimental measurements).

In order to understand the possible role of electric field for the stability, the complicated morphology of the liquid bridge in a quasistatic state [5] is approximately simplified as an axisymmetric or cylindrical liquid jet under an applied electric field. Then the model of an axial electrified jet [23,24] is employed here, and a phase diagram is obtained by the linear stability analysis.

A. Dispersion relationship

The linear stability analysis allows the investigation of its stability on the perturbation, giving rise to the following dispersion relation between the perturbation growth rate (ω) and the wavelength (k),

$$\omega = k \sqrt{\frac{1}{2}(1 - k^2) - \frac{\Omega^2}{4\pi} \left[1 + \frac{2}{\beta k^2 \ln(Bk)} \right]}, \quad (5)$$

in the limit of the infinite conductivity, zero viscosity, and zero surface charge [24]. Indeed this limit is applicable here, since the dimensionless conductivity is $K^* = K\sqrt{r^3\rho}/(\gamma\beta)/\bar{\epsilon} \sim 10^4$ and dimensionless viscosity $\mu^* = \sqrt{\mu}/(\rho\gamma r) \sim 10^{-3}$ (ρ for the density of water, r for the typical length scale, and μ for the kinetic viscosity of water). Here the dimensionless number $\beta = \epsilon/\bar{\epsilon} - 1$, the growth rate is nondimensionalized with timescale $\sqrt{\rho r^3/\gamma}$, whereas the dimensionless electrical field $\Omega = E/\sqrt{\gamma/[(\epsilon - \bar{\epsilon})r]}$, and $B = 0.89$ for a constant.

Based on Eq. (5), Fig. 7(a) presents this dispersion relation between the perturbation growth rate (ω) and the wavelength (k) under various dimensionless electric fields Ω . For each Ω , there is a maximum growth rate of ω (ω_{\max}) for the wavelength in the range from 0 to 1, and ω_{\max} decreases with Ω .

Then the maximum growth rate $\omega_{\max} = \max[\omega(k)]$ dependent on the electric field (Ω) is presented in Fig. 7(b). ω_{\max} gradually decreases with Ω due to the suppression of instability by the electric field, and eventually becomes zero associated with the marginal stability at $\Omega^* = 2.18$, indicating the transition from instability to stability.

B. Phase diagram

Then from the dimensionless Ω^* , the phase diagram between the critical electric field E^* and the radius r_0 [the blue line in Fig. 7(c)] is obtained as follows,

$$\Omega^* = E^*/\sqrt{\gamma/[(\epsilon - \bar{\epsilon})r_0]}. \quad (6)$$

To check the theory with experiments, both the aforementioned electric field at the initial formation ($E_{\text{formation}}$, the black line) and the final breakup (E_{breakup} , the red line) are indicated in

this phase diagram [Fig. 7(c)]. During the evolution of the liquid bridge within tens of minutes or hours, the electric field gradually decreases, while the diameter is reduced as well, consequently leading the transition from the stable regime at the initial stage (the dark square) to the unstable regime subjected to the final breakup (the red circle). Hence, the experiments are consistent with the theory well.

VII. DISCUSSION AND OUTLOOK

We have presented our experimental findings of the final fate of the Armstrong liquid bridge. Generally, this intriguing ALB is extremely complicated, and several more issues are still required to be further explored in future. First, although the observed effective length (\tilde{L}) associated with breakup is simple, the dynamics of climbing height (h) is determined by many complicated processes. For example, the current density leads to the elevated temperature due to the Joule heating, and the subsequent temperature-dependent evaporation causes the change of h . Also, other parameters (such as the axial flow of the liquid bridge and the accident water leakage) can affect h as well.

Second, during the evolution stage, the bidirectional axial flow was observed using magnetic resonance imaging [25], and was explained by the electro-osmotic flow due to the charges on the outer surface of the liquid bridge [21]. Here the axial flow in the liquid bridge is directly visualized by the “waterfall” from the thermal images [Fig. 3(b)], and its bidirectionality is clearly shown by the thermal video (see Supplemental Material [16] for Video 3) and the mass transport in the beakers (more details in Appendix B). Specifically, the maximum velocity [25] is comparable with the maximum flow velocity on the order of tens of millimeters per second [Fig. 9(b)]. Since the temperature gradient exists along the liquid bridge as seen from the thermal images, the thermocapillary Marangoni flow might be another possible mechanism for this axial flow.

Third, the simplified model of an electrified jet in Sec. VI mainly demonstrates the prerequisite electric field to stabilize the liquid bridge, in order to understand the correlation between the observed effective length with the breakup. For a more quantitative understanding, other effects including the aforementioned axial flow, the surface charges, and the excess ions in water (water splitting at the high voltage \sim kV [6,9,26–28]) are needed to be carefully examined in the model, which is beyond the scope of this work.

Fourth, from the microscopic perspective, the existence or survival of the ALB has been mainly attributed to the peculiarity of water molecules [29–33]. But this possible mechanism has been ruled out experimentally, since the water molecules do not exhibit the preferred orientation along the strong electric field in ALB from the measurement of neutron scattering, Raman scattering, and x-ray scattering data [34–36]. Actually, nonaqueous liquids (such as ethanol, glycerol) with a low electric conductivity and a relative high dielectric constant can also form the liquid bridge [37]. Nevertheless, here we identify that the breakup is directly correlated with an effective length (\tilde{L}) proportional to the applied voltage, implying that a threshold electric field (E_{breakup}) is necessary to sustain the liquid bridge or be responsible for its stability, although the microscopic mechanism requires more careful research in the future.

Lastly, many other factors might control the ALB as well. For example, the ambient environments (such as the temperature and humidity) affect the evaporation rate to influence the water loss and its lifetime. Likely, the surface tension can be decreased due to the ionized charges within the liquid bridge [38]. Additionally, the possible viscoelastic behavior and the related Young’s modulus can be induced by the applied strong electric field [39]. These more complicated parameters might inspire further investigations in the future.

In summary, we experimentally explore the formation, evolution, and breakup of the Armstrong liquid bridge, and report three main findings. First, the breakup occurs once an effective length (\tilde{L}) is reached, which is well reproduced under a given voltage and linearly increases with the applied voltage. Second, by introducing an external flow, the lifetime of the liquid bridge can be controlled,

while the effective length associated with the breakup is independent of the external flow rate. Hence, these experiments remarkably demonstrate that the final fate of the liquid bridge is directly correlated with the effective length. Third, in order to understand the observed stability and lifetime associated with the effective length, a simplified model of an electrified jet is employed by taking the electric field into account, and the linear stability analysis agrees with experiments well. These results provide a fresh perspective on the “century-old” Armstrong liquid bridge—a remarkable observation of the effective length \tilde{L} is directly correlated with the breakup, shedding light on its underlying physical mechanism.

ACKNOWLEDGMENTS

We are grateful for one of the anonymous referees who has provided many insightful comments and helpful suggestions to improve the manuscript. This work is supported by the National Program in China and startup from Fudan University.

APPENDIX A: INITIAL MORPHOLOGY UNDER VARIOUS L AND THE ASSOCIATED V_c

By changing the distance L between the two beakers, the morphology of the ALB right after formation is captured [Figs. 8(a)–8(d)]. A larger distance L requires a higher V_c , and the linear increase of V_c with L [Fig. 8(e)] indicates that a critical electric field is required to initiate the formation of the ALB ($E_{\text{formation}} \approx 1 \text{ kV mm}^{-1}$).

Theoretically, in order to deform the water surface for the ALB formation, the Maxwell stress due to the electric field should be comparable with the surface tension,

$$\epsilon\epsilon_0 E^2 \sim \gamma/\kappa^{-1}, \quad (\text{A1})$$

where $\gamma = 73 \times 10^{-3} \text{ N m}^{-1}$ is the surface tension of water, the relevant length scale $\kappa^{-1} = 2.76 \text{ mm}$ for the base diameter of the Taylor cone [Fig. 1(b) at 10 ms], ϵ for the relative dielectric constant of the liquid, and ϵ_0 for the vacuum permittivity [40]. Then the estimated critical electric field ($E \sim \sqrt{\gamma/\epsilon\epsilon_0\kappa^{-1}} \sim 1.64 \text{ kV mm}^{-1}$) is fairly consistent with the experimental value of $E_{\text{formation}}$.

For the typical electrocoalescence under an applied voltage [41,42], two droplets (with the diameter of hundreds of micrometers, and the distance about tens of micrometers) are deformed

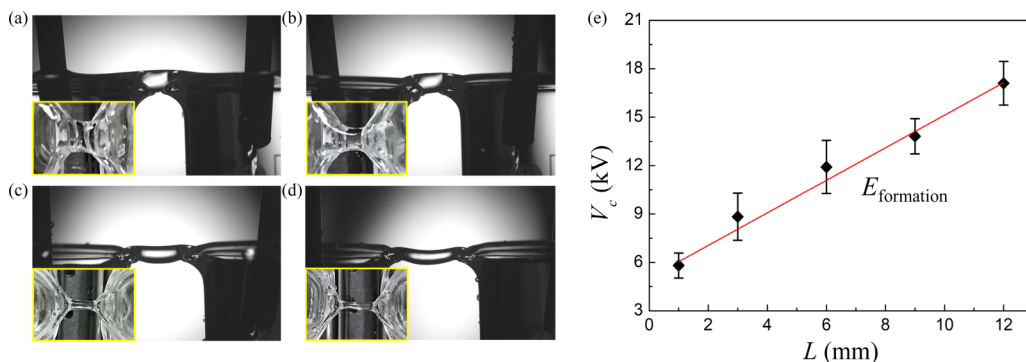


FIG. 8. Initial morphology under various L and the associated V_c . (a)–(d) A side view of the ALB morphology captured by the high-speed camera right after formation at the critical V_c for various L , while the inset (the yellow rectangular) for a top-down view from the digital camera, $L = 1, 3, 9, 12 \text{ mm}$, and $V_c = 6.0, 9.3, 14.7, 16.1 \text{ kV}$ for (a)–(d), respectively. (e) The critical voltage (V_c) increasing linearly with L , indicating a constant electric field ($E_{\text{formation}} = 1 \text{ kV mm}^{-1}$) required for the formation (error bars for fifteen measurements).

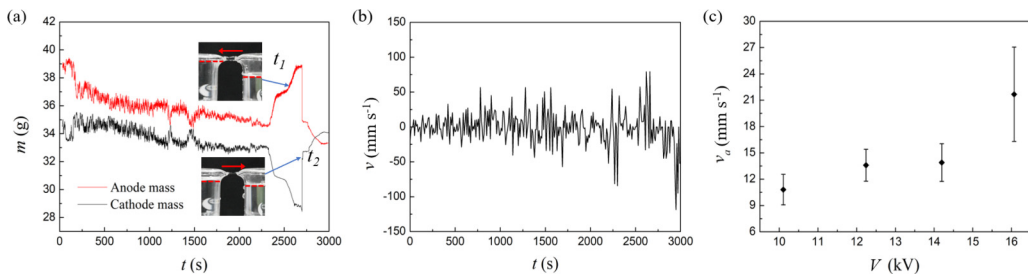


FIG. 9. Mass transport between two beakers via a bidirectional axial flow. (a) The mass changing at the anode and cathode sides over time under 12 kV. (b) The flow velocity fluctuating around tens of millimeters per second. (c) The average velocity increasing with the applied voltage, on the order of tens of millimeters per second. All the experiments are conducted with the fixed distance $L = 6$ mm and repeated four times ($L = 6$ mm).

and connected. Here this liquid bridge is suspended between two macroscopic beakers (with the diameter of centimeters, and distance about millimeters), which can last or be stable for a while involving much more complicated physical phenomena.

APPENDIX B: MASS TRANSPORT VIA AN AXIAL FLOW OF A WATERFALL

In order to measure the mass change of water in the beakers in the anode and cathode sides, two beakers are placed on two electronic balances (S1700689 JC-1202B), which are connected to computers to collect the data. The mass change with time on both sides is measured during the evolution of the ALB. As shown in Fig. 9(a), at time t_1 , the liquid mass in the anode side is larger and is still increasing (see the red arrow in the upper inset), while at time t_2 , there is a reversed flow of liquid from the anode side to the cathode side (see the red arrow in the lower inset), indicating a bidirectional flow during the evolution.

The flow velocity can be obtained from the mass change in Fig. 9(a). The rate of mass change is

$$dm/dt = \frac{(m_1^2 - m_2^2)/2 - (m_1^1 - m_2^1)/2}{t^2 - t^1}, \quad (\text{B1})$$

where m_i^j represents the mass at the time t^j in the beaker i ($i = 1, 2$ for the anode and cathode side, respectively). Then the flow velocity is

$$v = \frac{dm/dt}{\rho_w S^1}, \quad (\text{B2})$$

where ρ_w is the density of the liquid and S^1 is the area of the liquid bridge at the time t^1 . The flow velocity during the whole process fluctuates in the range of tens of millimeters per second as shown in Fig. 9(b). The time-averaged velocity $|v|$ (v_a), on the order of tens of millimeters per second, generally has a tendency to increase with the voltage [Fig. 9(c)].

-
- [1] W. G. Armstrong, *The Electrical Engineer* (The Newcastle Literary and Philosophical Society, New Castle, 1893), pp. 154–155.
 [2] E. C. Fuchs, J. Woisetschlager, K. Gatterer, E. Maier, R. Pecnik, G. Holler, and H. Eisenkolbl, The floating water bridge, *J. Phys. D: Appl. Phys.* **40**, 6112 (2007).
 [3] E. Hand, Water doesn't mind the gap, *Nature (London)* **449**, 517 (2007).
 [4] E. C. Fuchs, K. Gatterer, G. Holler, and J. Woisetschlager, Dynamics of the floating water bridge, *J. Phys. D: Appl. Phys.* **41**, 185502 (2008).

- [5] K. Morawetz, Theory of water and charged liquid bridges, *Phys. Rev. E* **86**, 026302 (2012); **86**, 069904(E) (2012).
- [6] M. Sammer, A. D. Wexler, P. Kuntke, H. Wiltse, N. Stanulewicz, E. Lankmayr, J. Woisetschlager, and E. C. Fuchs, Proton production, neutralisation and reduction in a floating water bridge, *J. Phys. D: Appl. Phys.* **48**, 415501 (2015).
- [7] E. C. Fuchs, D. Yntema, and J. Woisetschlager, Raman spectroscopy and shadowgraph visualization of excess protons in high-voltage electrolysis of pure water, *J. Phys. D: Appl. Phys.* **52**, 365302 (2019).
- [8] E. C. Fuchs, L. L. F. Agostinho, M. Eisenhut, and J. Woisetschlager, Mass and charge transfer within a floating water bridge, *Proc. SPIE* **7376**, 73761E (2010).
- [9] J. Woisetschlager, K. Gatterer, and E. C. Fuchs, Experiments in a floating water bridge, *Exp. Fluids* **48**, 121 (2010).
- [10] J. R. Melcher and G. I. Taylor, Electrohydrodynamics: A review of the role of the interfacial shear stresses, *Annu. Rev. Fluid Mech.* **1**, 111 (1969).
- [11] D. A. Saville, Electrohydrodynamics: The Taylor-Melcher leaky dielectric model, *Annu. Rev. Fluid Mech.* **29**, 27 (1997).
- [12] A. Widom, J. Swain, J. Silverberg, S. Sivasubramanian, and Y. N. Srivastava, Theory of the Maxwell pressure tensor and the tension in a water bridge, *Phys. Rev. E* **80**, 016301 (2009).
- [13] A. A. Aerov, Why the water bridge does not collapse, *Phys. Rev. E* **84**, 036314 (2011).
- [14] R. M. Namin, S. A. Lindi, A. Amjadi, N. Jafari, and P. Irajizad, Experimental investigation of the stability of the floating water bridge, *Phys. Rev. E* **88**, 033019 (2013).
- [15] A. D. Wexler, M. Lopez Saenz, O. Schreer, J. Woisetschlager, and E. C. Fuchs, The preparation of electrohydrodynamic bridges from polar dielectric liquids, *J. Vis. Exp.* **91**, e51819 (2014).
- [16] See Supplemental Material at <http://link.aps.org/supplemental/10.1103/PhysRevFluids.6.093901> for the high-speed videos of the ALB formation, evolution and breakup and the thermal video during the evolution.
- [17] G. I. Taylor, Disintegration of water drops in an electric field, *Proc. R. Soc. A* **280**, 383 (1964).
- [18] M. Cloupeau and B. Prunet-Foch, Electrostatic spraying of liquids in cone-jet mode, *J. Electrostat.* **22**, 135 (1989).
- [19] A. G. Marin and D. Lohse, Building water bridges in air: Electrohydrodynamics of the floating water bridge, *Phys. Fluids* **22**, 122104 (2010).
- [20] E. C. Fuchs, A. Cherukupally, A. H. Paulitsch-Fuchs, L. L. F. Agostinho, A. D. Wexler, J. Woisetschlager, and F. T. Freund, Investigation of the mid-infrared emission of a floating water bridge, *J. Phys. D: Appl. Phys.* **45**, 475401 (2012).
- [21] K. Morawetz, Reversed currents in charged liquid bridges, *Water* **9**, 353 (2017).
- [22] K. Hisatake, S. Tanaka, and Y. Aizawa, Evaporation rate of water in a vessel, *J. Appl. Phys.* **73**, 7395 (1993).
- [23] D. A. Saville, Electrohydrodynamic stability: Fluid cylinders in longitudinal electric fields, *Phys. Fluids* **13**, 2987 (1970).
- [24] M. M. Hohman, M. Shin, G. Rutledge, and M. P. Brenner, Electrospinning and electrically forced jets. I. Stability theory, *Phys. Fluids* **13**, 2201 (2001).
- [25] A. Wexler, S. Drusova, E. Fuchs, J. Woisetschlager, G. Reiter, M. Fuchsjager, and U. Reiter, Magnetic resonance imaging of flow and mass transfer in electrohydrodynamic liquid bridges, *J. Visualized Exp.* **20**, 97 (2017).
- [26] E. C. Fuchs, M. Sammer, A. D. Wexler, P. Kuntke, and J. Woisetschlager, A floating water bridge produces water with excess charge, *J. Phys. D: Appl. Phys.* **49**, 125502 (2016).
- [27] O. Teschke, J. R. D. Castro, J. F. V. Filho, and D. M. Soares, Protonic charge defect structures in floating water bridges observed as Zundel and Eigen solvation arrangements, *Chem. Phys. Lett.* **685**, 239 (2017).
- [28] O. Teschke, J. R. D. Castro, J. F. V. Filho, and D. M. Soares, Hydrated excess proton Raman spectral densities probed in floating water bridges, *ACS Omega* **3**, 13977 (2018).
- [29] E. C. Fuchs, Can a century old experiment reveal hidden properties of water? *Water* **2**, 381 (2010).
- [30] E. C. Fuchs, A. D. Wexler, A. H. Paulitsch-Fuchs, L. L. F. Agostinho, D. Yntema, and J. Woisetschlager, The Armstrong experiment revisited, *Eur. Phys. J. Special Topics* **223**, 959 (2014).

- [31] C. Q. Sun, Water electrification: Principles and applications, *Adv. Colloid Interface Sci.* **282**, 102188 (2020).
- [32] E. Del Giudice, E. C. Fuchs, and G. Vitiello, Collective molecular dynamics of a floating water bridge, *Water* **2**, 69 (2010).
- [33] E. Del Giudice and G. Vitiello, Influence of gravity on the collective molecular dynamics of liquid water: The case of the floating water bridge, *Water* **2**, 133 (2011).
- [34] E. C. Fuchs, B. Bitschnau, J. Woisetschlager, E. Maier, B. Beuneu, and J. Teixeira, Neutron scattering of a floating heavy water bridge, *J. Phys. D: Appl. Phys.* **42**, 65502 (2009).
- [35] R. C. Ponterio, M. Pochylski, F. Aliotta, C. Vasi, M. E. Fontanella, and F. Saija, Raman scattering measurements on a floating water bridge, *J. Phys. D: Appl. Phys.* **43**, 175405 (2010).
- [36] L. B. Skinner, C. J. Benmore, B. Shyam, J. K. R. Weber, and J. B. Parise, Structure of the floating water bridge and water in an electric field, *Proc. Natl. Acad. Sci. USA* **109**, 16463 (2002).
- [37] J. Woisetschlager, A. D. Wexler, G. Holler, M. Eisenhut, K. Gatterer, and E. C. Fuchs, Horizontal bridges in polar dielectric liquids, *Exp. Fluids* **52**, 193 (2012).
- [38] O. Teschke, D. M. Soares, W. E. Gomes, and J. F. V. Filho, Floating liquid bridge charge dynamics, *Phys. Fluids* **28**, 012105 (2016).
- [39] O. Teschke, D. M. Soares, and J. F. V. Filho, Floating liquid bridge tensile behavior: Electric-field-induced Young's modulus measurements, *Appl. Phys. Lett.* **103**, 251608 (2013).
- [40] P. Kim, C. Duprat, S. S. H. Tsai, and H. A. Stone, Selective Spreading and Jetting of Electrically Driven Dielectric Films, *Phys. Rev. Lett.* **107**, 034502 (2011).
- [41] J. C. Bird, W. D. Ristenpart, A. Belmonte, and H. A. Stone, Critical Angle for Electrically Driven Coalescence of Two Conical Droplets, *Phys. Rev. Lett.* **103**, 164502 (2009).
- [42] G. Chen, P. Tan, S. Chen, J. Huang, W. Wen, and L. Xu, Coalescence of Pickering Emulsion Droplets Induced by an Electric Field, *Phys. Rev. Lett.* **110**, 064502 (2013).